# Encoding Higher-Order Polarization States into Robust Partially Coherent Optical Beams

Zhen Dong,[1] Yahong Chen,[1,*] Fei Wang,[1] Yangjian Cai,[1,2,†] Ari T. Friberg,[3] and Tero Setälä[3,‡]

[1] *School of Physical Science and Technology, Soochow University, Suzhou 215006, China*

[2] *Shandong Provincial Engineering and Technical Center of Light Manipulation & Shandong Provincial Key Laboratory of Optics and Photonic Devices, School of Physics and Electronics, Shandong Normal University, Jinan 250014, China*

[3] *Institute of Photonics, University of Eastern Finland, P.O. Box 111, Joensuu FI-80101, Finland*

(Received 26 April 2022; revised 16 June 2022; accepted 8 August 2022; published 14 September 2022)

Optical vector beams with a higher-order polarization state, represented by a point on a higher-order Poincaré sphere, have recently found advantages in various applications. However, the considered beams are usually spatially fully coherent (monochromatic), which makes them susceptible to complex environments. In this work, we introduce a coherence-engineering protocol to generate partially coherent vectorial secondary light sources in which a higher-order polarization state is encoded into the structure of electromagnetic spatial coherence. The encoded complex polarization state is well reconstructed in the far field whose global degree of polarization can be controlled with the transverse coherence length of the source. In particular, the produced partially coherent beams are highly robust against obstructions, which is demonstrated theoretically and experimentally by inserting a static obstacle against the source or introducing strong atmospheric turbulence into the transmission link. The results of this work can find useful applications in the transfer of complicated polarization-encoded information in harsh environments.

DOI: 10.1103/PhysRevApplied.18.034036

## I. INTRODUCTION

Polarization is a fundamental characteristic of light and a key attribute in various situations including, e.g., optical imaging, three-dimensional displays, and remote sensing [1]. Optical vector beams with spatially nonuniform polarization states [2,3] have attracted considerable attention during the past two decades due to the extraordinary properties they show when interacting with matter. This has led to a wide array of applications, from superresolution imaging [4,5] and optical trapping [6] to optical communications [7,8], high-dimensional quantum cryptography [9,10], and classical entanglement [11,12]. A particularly useful class of nonuniform polarization states is represented by the points on the higher-order Poincaré spheres [13]. These higher-order polarization states can be viewed as superpositions of two basic modes with opposite spin (circular polarization) and orbital angular momenta (helicity). A beam in a higher-order polarization state can be synthesized by superimposing two orthogonally polarized fields that have been individually shaped beforehand with a computer-generated hologram [14] or created with the geometric-phase-controlled metasurface elements such as the q-plate [15,16] or J-plate [17]. It has also been shown that the higher-order polarization states can be generated directly from a laser with an intracavity geometric phase control [18].

However, the above methods of beam production exploit spatially fully coherent light and the generated higher-order polarization states are carried by spatially coherent light beams. Thus, the polarization states can be highly sensitive to disturbances in the propagation path even though vector beams are more robust to perturbations than scalar beams, which correspond to uniform polarization [19,20]. In addition, when a vector beam propagates through an atmospheric turbulence, the polarization state suffers from beam wander and Stokes-parameter scintillations induced by the fluctuations of the refractive index of turbulence. This distorts the polarization profile, the stronger the turbulence strength is [21–23]. Although adaptive optics [24–26] and polarization-encoding methods [27] have been used to compensate for distortions caused by weak turbulence, yet it remains a challenge to overcome the beam distortions caused by a strong turbulence. Undeteriorated transmission of high-quality complex polarization states in harsh environments could find great advantages in high-speed information transfer and real-time polarization imaging and trapping through complex media.

*yahongchen@suda.edu.cn
†yangjiancai@suda.edu.cn
‡tero.setala@uef.fi

 

Spatial coherence engineering [28] refers to the control of the two-point (second-order) statistical properties of random light rather than the one-point deterministic qualities considered in the approaches involving fully coherent (monochromatic) light. Random light beams with controlled states of spatial coherence have found use in many applications including sub-Rayleigh imaging [29], robust microscopy imaging [30], beam shaping [31], optical encryption [32], and robust far-field image transmission [33,34]. In this work, we put forward a coherence-engineering variant to generate partially spatially coherent vectorial secondary sources in which a higher-order polarization state is encoded into the spatial coherence properties. We demonstrate theoretically and experimentally that a high-quality reconstruction of the polarization state ensues in the far zone where the global degree of polarization can be controlled by the transverse coherence length of the source. We further show that due to the partial spatial coherence the constructed beams are highly robust against obstructions such as a large obstacle or strong turbulence.

## II. HIGHER-ORDER POLARIZATION STATES

Throughout this section we consider a monochromatic light beam with time dependence $\exp(-i\omega t)$, where $\omega$ is the angular frequency. However, the explicit frequency dependence of the various quantities is not shown. A beam in a higher-order polarization state can be represented by a point on a higher-order Poincaré (HOP) sphere with the poles corresponding to the circularly polarized beams (right-hand circular at the north pole and left-hand circular at the south pole) with opposite helical wave fronts [13]. The helicity of the wave front arises from the azimuthally varying phase factor $\exp(il\varphi)$, where $\varphi$ is the azimuthal angle and $l$ is the topological charge of the vortex phase, which can take any integer value. The complex vector amplitudes of the light beams at the north and south poles are given by $\mathbf{E}_N(\mathbf{r}) = E_0\mathcal{L}_{0,l}(\mathbf{r})\hat{\mathbf{e}}_R$ and $\mathbf{E}_S(\mathbf{r}) = E_0\mathcal{L}_{0,-l}(\mathbf{r})\hat{\mathbf{e}}_L$, respectively, where $E_0$ is a complex coefficient specifying the amplitude and $\hat{\mathbf{e}}_R = (\hat{\mathbf{e}}_x + i\hat{\mathbf{e}}_y)/\sqrt{2}$, $\hat{\mathbf{e}}_L = (\hat{\mathbf{e}}_x - i\hat{\mathbf{e}}_y)/\sqrt{2}$ with $\hat{\mathbf{e}}_x$ and $\hat{\mathbf{e}}_y$ being the Cartesian unit vectors in the $x$-$y$ plane. The fields are Laguerre-Gaussian beams whose spatial profiles at the waist plane are written as

$$\mathcal{L}_{p,\pm l}(\mathbf{r}) = \sqrt{\frac{2p!}{\pi(p+|l|)!}}\left(\frac{\sqrt{2}r}{w_0}\right)^{|l|}\exp\left(-\frac{r^2}{w_0^2}\right) \times L_p^{|l|}\left(\frac{2r^2}{w_0^2}\right)\exp(\pm il\varphi), \quad (1)$$

where $L_p^{|l|}(\cdot)$ is the generalized Laguerre polynomial, $w_0$ the waist radius, and $(r,\varphi)$ are the polar coordinates.

The field located at a point on a higher-order Poincaré sphere, with the order specified by $l$, can be expressed as a superposition of $\mathbf{E}_N(\mathbf{r})$ and $\mathbf{E}_S(\mathbf{r})$ [35,36], i.e.,

$$\mathbf{E}(\mathbf{r}) = \cos\left(\frac{\Theta}{2}\right)e^{-i\frac{\Phi}{2}}\mathbf{E}_N(\mathbf{r}) + \sin\left(\frac{\Theta}{2}\right)e^{i\frac{\Phi}{2}}\mathbf{E}_S(\mathbf{r}), \quad (2)$$

where $\Theta \in [0,\pi]$ and $\Phi \in [0,2\pi)$ are the polar and azimuthal angles, respectively, in the spherical polar coordinates (see Fig. 1). In general, for any order $l$ the beams characterized by Eq. (2) are uniformly circularly polarized at the poles but nonuniformly polarized elsewhere. The polarization state can be adjusted by altering $\Theta$ and $\Phi$. The former controls the ellipticity of the polarization ellipse whereas the latter affects its orientation at a fixed spatial point in a higher-order state. On the equator of the HOP sphere ($\Theta = \pi/2$), all polarization ellipses collapse into linear polarization states with various orientations. We note that the famous class of cylindrical vector beams [2] are located on the equator of the HOP sphere with order $l = 1$. As an example, Fig. 1 shows the polarization states (and the intensity distributions) for some beams located at different points on the HOP sphere of order $l = 3$.

The traditional representation of a polarization state takes place via the four Stokes parameters defined as [37,38]

$$S_j(\mathbf{r}) = \mathrm{tr}[\boldsymbol{\sigma}_j\boldsymbol{\Phi}(\mathbf{r})], \quad j \in (0,\ldots,3), \quad (3)$$

where tr denotes the matrix trace and $\boldsymbol{\Phi}(\mathbf{r}) = \mathbf{E}^*(\mathbf{r})\mathbf{E}^T(\mathbf{r})$ is the polarization matrix (of a monochromatic beam), with

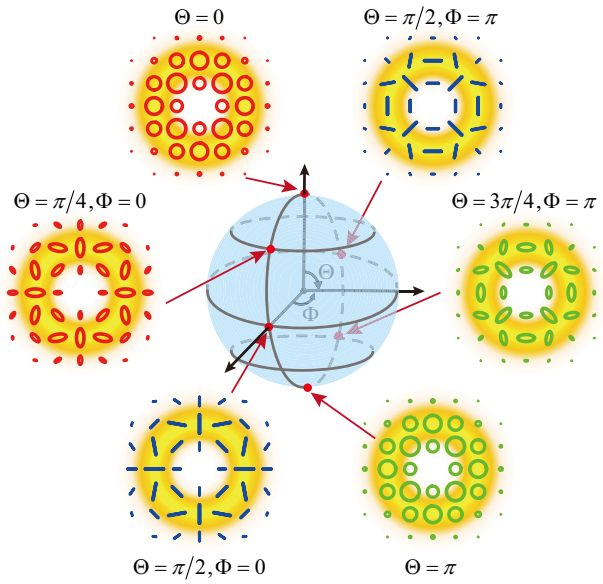


FIG. 1. Illustration of the Poincaré sphere of order $l = 3$ where $\Theta$ and $\Phi$ are the polar and azimuthal angles of the spherical coordinates. Blue short lines, linear polarizations; red ellipses, right-hand elliptical polarizations; green ellipses, left-hand elliptical polarizations.

the asterisk and superscript $T$ denoting the complex conjugate and matrix transpose, respectively. Further, $\boldsymbol{\sigma}_0$ is the $2 \times 2$ unit matrix, and $\boldsymbol{\sigma}_1$, $\boldsymbol{\sigma}_2$, and $\boldsymbol{\sigma}_3$ are the three Pauli matrices [38]. Notice that for a higher-order polarization state the Stokes parameters constitute, in general, nonuniform distributions.

To assess the robustness of a higher-order polarization state against complex environments, below we analyze theoretically and experimentally the beam propagation through a link, which includes a static obstacle or exhibits fluctuating turbulence. The first case relies on the Huygens-Fresnel diffraction integral formula while the second situation is based on the multiphase screen method [39]. Both methods are described within the Supplemental Material [40], where also the experimental generation of the higher-order polarization states is described. In the experiment, a common path interferometric arrangement [41] is used to synthesize two optical modes with opposite spin and helical wave fronts [42].

### A. Static obstacle in the beam

In this subsection, we analyze with simulations and experiments the reconstruction of a monochromatic (hence fully polarized and spatially fully coherent) beam in a higher-order polarization state when a sector-shaped obstruction of closing angle $\phi$ blocks a part of the beam in the source plane. The polarization state corresponds to the point $\Theta = \pi/2$ and $\Phi = 0$ on the HOP sphere of order $l = 3$. The wavelength of light is chosen as $\lambda = 532$ nm and the waist radius is $w_0 = 1$ mm. The intensity and polarization state are then recorded in the focal plane of a lens placed against the obstacle and having a focal length of 400 mm. Figure 2 shows the simulated focal-plane intensity and polarization-state distributions for various closing angles of the obstacle. In (a) the distributions without an obstacle are shown and apart from a scaling due to the lens, they are the same as those in the source plane (see case $\Theta = \pi/2$, $\Phi = 0$ in Fig. 1). The distributions remain unchanged on propagation because the beam is synthesized as a linear superposition of two fundamental Laguerre-Gaussian modes with identical Gouy phases [43]. For small closing angles ($\phi = \pi/8$ and $\pi/4$), the intensity and polarization state in the focal plane differ only slightly from those without the obstruction. As the angle $\phi$ increases, the ring-shaped intensity distribution becomes asymmetric and the ellipticities and orientations of the local polarization ellipses start to deviate from those of the source. For $\phi = 7\pi/4$, i.e., 87.5% of the beam area is blocked in the source plane, the intensity and polarization state in the output plane no longer reflect the original distributions. Figure 3 shows the measured Stokes parameters [normalized by the maximum value of $S_0(\mathbf{r})$] as well as the polarization ellipses in the focal plane in the absence of obstacle [(a)–(d)] and when an obstruction with $\phi = 7\pi/4$ is present [(e)–(h)]. The experimental results are in agreement with the theoretical predictions, i.e., with a large obstacle in the propagation link, the polarization state of the source cannot be recovered in the focal plane.

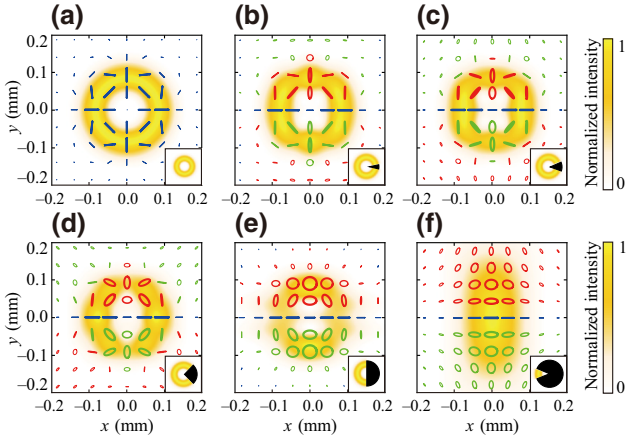


FIG. 2. Simulated focal-plane intensity and polarization-state distributions for a focused beam in a higher-order polarization state ($\Theta = \pi/2$, $\Phi = 0$, and $l = 3$). The beam source is blocked by a sector-shaped obstacle (see inset) having the closing angle of (a) $\phi = 0$, (b) $\phi = \pi/8$, (c) $\phi = \pi/4$, (d) $\phi = \pi/2$, (e) $\phi = \pi$, and (f) $\phi = 7\pi/4$.

### B. Propagation through a turbulent medium

Next, we study the robustness of a higher-order polarization state against propagation through a fluctuating turbulence. In the simulations, we assume that the turbulence obeys Kolmogorov statistics and adopt the (modified) von Kármán power spectrum for the index-of-refraction fluctuations [44], i.e.,

$$\Phi_n(\kappa) = 0.033 C_n^2 (\kappa^2 + \kappa_0^2)^{-11/6} \exp(-\kappa^2/\kappa_m^2), \qquad (4)$$

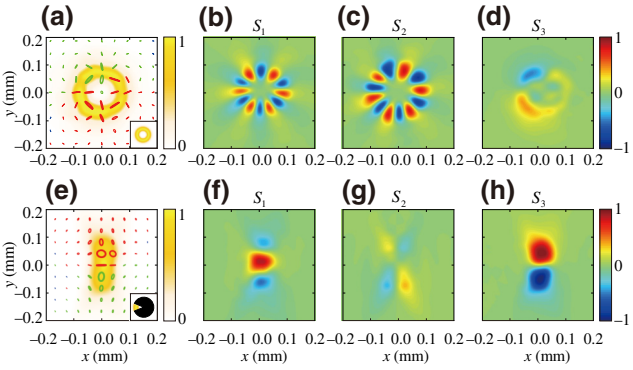


FIG. 3. Measured focal-plane intensity, polarization ellipse, and Stokes-parameter distributions for the same beam as in Fig. 2: (a)–(d) without an obstacle, and (e)–(h) with an obstacle of $\phi = 7\pi/4$.

where $C_n^2$ is the generalized refractive-index structure parameter. Further, $\kappa_0 = 2\pi/L_0$ and $\kappa_m = 5.92/l_0$ with $L_0$ and $l_0$ being the outer and inner scale of the turbulence for which we choose $L_0 = 1$ m, $l_0 = 1$ mm. The strength of the turbulence can be determined by the Rytov variance, $\sigma_R^2 = 1.23 C_n^2 k^{7/6} z^{11/6}$ where $z$ is the propagation distance which is taken to be 1 m. For weak turbulence $\sigma_R^2 < 1$ while for moderate and strong turbulences $\sigma_R^2 \geq 1$. In this work, $C_n^2 = 5 \times 10^{-10}$ m$^{-2/3}$ and $C_n^2 = 5 \times 10^{-9}$ m$^{-2/3}$ are selected for the cases of the weak turbulence ($\sigma_R^2 \approx 0.11$) and strong turbulence ($\sigma_R^2 \approx 1.1$), respectively. After propagation through the turbulence, the beam is focused by a thin lens of focal length 400 mm placed directly after the turbulence section (1 m distance from the source).

Figure 4 depicts the simulated instantaneous intensity and polarization-state distributions in the focal plane for a beam with $\Theta = \pi/2$, $\Phi = 0$, and $l = 3$ propagated through the weak and strong turbulences. As shown in (a)–(d), both distributions are effectively stable under the weak turbulence. However, in the case of strong turbulence, the intensity and polarization-state distributions become distorted [see (e)–(h)] and unstable with large beam wander. To demonstrate the instability experimentally, we let the beam pass through a thermal turbulence generated by a hot graphitic plate with temperature 200 °C. Figure 5 shows the recorded intensities (transmitted by a linear polarizer in the $x$ direction) in the focal plane at four instants of time. It is found that the six-petal intensity distribution is distorted and the beam spot becomes unstable due to the turbulence, suggesting variations in both the polarization state and intensity. We note that the beam wander in the experiments is less than in the simulations [Figs. 4(e)–4(h)]

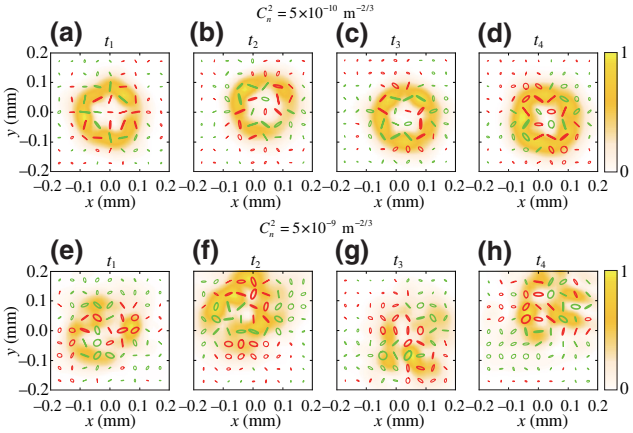


FIG. 4. Simulated focal-plane intensity and polarization-state distributions for a beam with $\Theta = \pi/2$, $\Phi = 0$, and $l = 3$ after propagating a distance of 1 m in an atmospheric turbulence. (a)–(d) $C_n^2 = 5 \times 10^{-10}$ m$^{-2/3}$ (weak turbulence), and (e)–(h) $C_n^2 = 5 \times 10^{-9}$ m$^{-2/3}$ (strong turbulence) at four instants of time. The intensity distributions are normalized by the maximum value.

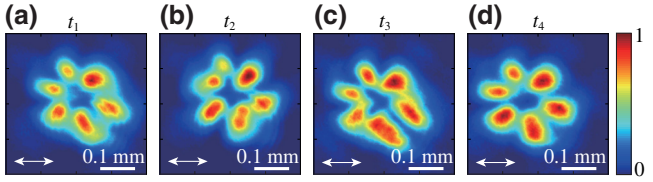


FIG. 5. Measured instantaneous focal-plane intensity distributions of the beam with $\Theta = \pi/2$, $\Phi = 0$, and $l = 3$ propagated through a thermal turbulence generated by a graphitic plate in 200 °C temperature. The results are for the $x$ component of the field whose direction is indicated with the arrow. The distributions are normalized by the maximum intensity.

since the thermally induced turbulence in the former case is weaker than the atmospheric turbulence with $C_n^2 = 5 \times 10^{-9}$ m$^{-2/3}$ in the latter situation.

## III. ROBUST HIGHER-ORDER POLARIZATION STATES

In this section, we outline how a robust higher-order polarization state is generated in terms of the spatial coherence engineering of a partially coherent secondary light source. We examine both theoretically and experimentally the robustness of the state by passing the beam with designed partial spatial coherence through a transmission link containing a large obstruction or strong fluctuating turbulence.

### A. Spatial coherence engineering

The second-order statistical properties of a partially coherent vectorial light beam in the space-frequency domain are contained in the cross-spectral density matrix, defined as [37,38]

$$\mathbf{W}(\mathbf{r}_1, \mathbf{r}_2) = \langle \boldsymbol{\mathcal{E}}^*(\mathbf{r}_1) \boldsymbol{\mathcal{E}}^T(\mathbf{r}_2) \rangle, \tag{5}$$

where $\boldsymbol{\mathcal{E}}(\mathbf{r})$ is a monochromatic field realization and the angle brackets denote the ensemble average. In order to control the spatial coherence properties of a source beam, we decompose the four elements of the cross-spectral density matrix in the following integral form [45]:

$$W_{\alpha\beta}(\mathbf{r}_1, \mathbf{r}_2) = \int p_{\alpha\beta}(\mathbf{v}) H_\alpha^*(\mathbf{r}_1, \mathbf{v}) H_\beta(\mathbf{r}_2, \mathbf{v}) d^2\mathbf{v}, \tag{6}$$

with $(\alpha, \beta) \in (x, y)$. Above, $H_x(\mathbf{r}, \mathbf{v})$ and $H_y(\mathbf{r}, \mathbf{v})$ are generally two arbitrary kernels that connect the weighting-matrix elements $p_{\alpha\beta}(\mathbf{v})$ in the $\mathbf{v}$ domain and the cross-spectral density in the $\mathbf{r}$ domain.

To obtain a genuine coherence matrix, $p_{\alpha\beta}(\mathbf{v})$ must obey the non-negative definiteness condition [45]

$$p_{xx}(\mathbf{v}) \geq 0,\ p_{yy}(\mathbf{v}) \geq 0,\ p_{xx}(\mathbf{v}) p_{yy}(\mathbf{v}) \geq |p_{xy}(\mathbf{v})|^2. \tag{7}$$

Due to the fact that $\mathbf{W}(\mathbf{r}_1, \mathbf{r}_2) = \mathbf{W}^\dagger(\mathbf{r}_2, \mathbf{r}_1)$, where the dagger denotes the Hermitian adjoint, the weighting matrix $p_{\alpha\beta}(\mathbf{v})$ is necessarily purely Hermitian. These two features indicate that $p_{\alpha\beta}(\mathbf{v})$ has the same mathematical properties as the polarization matrix, $\mathbf{\Phi}(\mathbf{r}) = \mathbf{W}(\mathbf{r}, \mathbf{r})$, of a light beam. Indeed, as we see $p_{\alpha\beta}(\mathbf{v})$ coincides with the polarization matrix of the beam whose polarization information is encoded into the state of electromagnetic spatial coherence. Practical implementation of this procedure for a beam with a higher-order polarization state is discussed within the Supplemental Material [40]. Later we show that the encoded polarization state can be accurately recovered in the far zone or in the focal plane of a thin lens. In other words, we can create a far-field polarization state by engineering the beam's spatial coherence properties in the source plane via Eq. (6).

In the experiments [40], the encoding of polarization information into spatial coherence characteristics is based on the generalized van Cittert-Zernike theorem [32,46]. Firstly, a spatially fully coherent beam in a higher-order polarization state is rendered spatially incoherent using a dynamic diffuser [47], e.g., a rotating ground-glass disk (RGGD). The beam is subsequently transmitted through an optical system composed of a thin lens at the focal length distance from the RGGD followed by a closely placed Gaussian amplitude filter (GAF) that controls the intensity distribution. The related response functions (kernels) $H_x(\mathbf{r}, \mathbf{v})$ and $H_y(\mathbf{r}, \mathbf{v})$ for the $x$ and $y$ field components are given by

$$H_x(\mathbf{r}, \mathbf{v}) = H_y(\mathbf{r}, \mathbf{v}) = T(\mathbf{r}) \frac{-i \exp(ikf)}{\lambda f} \exp\left[\frac{i\pi}{\lambda f}(\mathbf{v}^2 - 2\mathbf{r}\cdot\mathbf{v})\right], \quad (8)$$

where $\lambda$ is the wavelength of light, $f$ the focal length of the lens, and $\mathbf{r}$ and $\mathbf{v}$ refer to spatial points in the GAF and RGGD planes, respectively. In addition, $T(\mathbf{r}) = \exp[-\mathbf{r}^2/(2\sigma_0)^2]$ denotes the transmission function of the GAF with $\sigma_0$ specifying the width of the engineered beam. We let $\sigma_0 = 1$ mm in the following simulation and experiment to confirm that the beam dimensions for the partially coherent and fully coherent beams are the same.

Inserting Eq. (8) into Eq. (6), the cross-spectral density matrix of the tailored (secondary) source beam can be expressed as

$$W_{\alpha\beta}(\mathbf{r}_1, \mathbf{r}_2) = K_{\alpha\beta} T(\mathbf{r}_1) T(\mathbf{r}_2) \mu_{\alpha\beta}(\mathbf{r}_1 - \mathbf{r}_2), \quad (9)$$

where we use the fact that $T(\mathbf{r})$ is real. In addition,

$$K_{\alpha\beta} = \frac{1}{(\lambda f)^2}\left[\int p_{\alpha\alpha}(\mathbf{v}) d^2\mathbf{v} \int p_{\beta\beta}(\mathbf{v}) d^2\mathbf{v}\right]^{1/2}, \quad (10)$$

ensures that

$$\mu_{\alpha\beta}(\mathbf{r}_1 - \mathbf{r}_2) = \frac{1}{K_{\alpha\beta}} \int \frac{p_{\alpha\beta}(\mathbf{v})}{(\lambda f)^2} \exp\left[\frac{i2\pi\mathbf{v}\cdot(\mathbf{r}_1 - \mathbf{r}_2)}{\lambda f}\right] d^2\mathbf{v}, \quad (11)$$

is the normalized correlation function (correlation coefficient) of the $\alpha$ and $\beta$ field components at $\mathbf{r}_1$ and $\mathbf{r}_2$. We see that the spatial distributions of the correlation coefficients are given by the Fourier transforms of the polarization-matrix elements of the encoded state. The spatial coherence width, a measure of the effective width of the correlation coefficients, of the generated source is determined by both the size of the beam spot ($w_0$) on the RGGD and the focal length $f$. Based on Eq. (11), we notice that the coherence width decreases with increasing $w_0$ and decreasing $f$.

We use the recently introduced generalized Hanbury Brown-Twiss approach [48] to measure the normalized spatial correlation functions in the plane just after the amplitude filter. The functions are found to be real valued although they generally are complex quantities. Figures 6(a)–6(c) depict the measured correlation distributions for the encoded higher-order beam of $\Theta = \pi/2$, $\Phi = 0$, and $l = 3$. We see that the two-point spatial correlations express the six-petal distributions similar to those of the one-point Stokes parameters in Figs. 3(b)–3(d). We verify numerically that Figs. 3 and 6 are consistent with Eq. (11) showing that the polarization state is encoded in the second-order spatial coherence of a partially coherent vector beam. Remarkably, it is also found that the beam itself is completely unpolarized with the degree of polarization [38]

$$P(\mathbf{r}) = \left[1 - \frac{4\det\mathbf{\Phi}(\mathbf{r})}{\mathrm{tr}^2\mathbf{\Phi}(\mathbf{r})}\right]^{1/2}, \quad (12)$$

being equal to zero in every point (det refers to determinant). In general, $P(\mathbf{r})$ represents the ratio of the spectral density of the fully polarized constituent to the total spectral density when the polarization matrix is decomposed into unpolarized and fully polarized parts [38]. The fact that $P(\mathbf{r}) = 0$ is confirmed by the measured electromagnetic degree of coherence depicted in Fig. 6(d). The degree of coherence of electromagnetic beams is defined as [37,49]

$$\mu(\mathbf{r}_1, \mathbf{r}_2) = \left[\frac{\mathrm{tr}[\mathbf{W}^\dagger(\mathbf{r}_1, \mathbf{r}_2)\mathbf{W}(\mathbf{r}_1, \mathbf{r}_2)]}{\mathrm{tr}\mathbf{W}(\mathbf{r}_1, \mathbf{r}_1)\mathrm{tr}\mathbf{W}(\mathbf{r}_2, \mathbf{r}_2)}\right]^{1/2}, \quad (13)$$

whose equal-point value is seen to be $\mu^2(\mathbf{r}, \mathbf{r}) = 0.5$. With the help of the relation $P^2(\mathbf{r}) = 2[\mu^2(\mathbf{r}, \mathbf{r}) - 0.5]$ [49], we obtain $P(\mathbf{r}) = 0$. We show later that upon propagation the

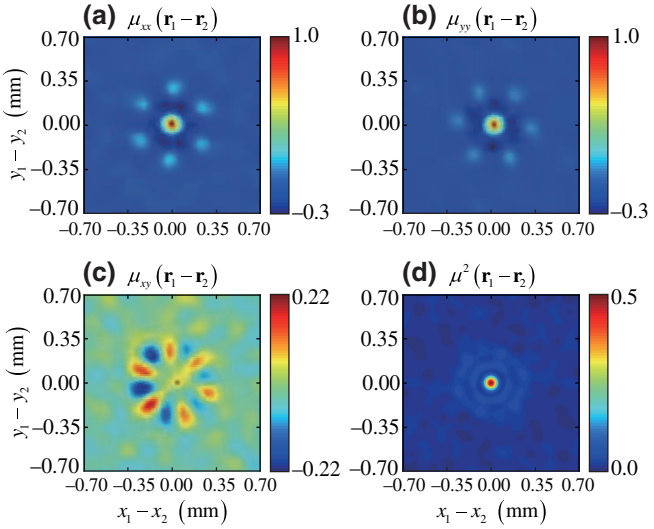


FIG. 6. Measured spatial distributions of the normalized correlation functions $\mu_{xx}(\mathbf{r}_1-\mathbf{r}_2)$, $\mu_{yy}(\mathbf{r}_1-\mathbf{r}_2)$, and $\mu_{xy}(\mathbf{r}_1-\mathbf{r}_2)$, as well as the electromagnetic degree of coherence $\mu^2(\mathbf{r}_1-\mathbf{r}_2)$ for the synthesized partially coherent vector source. The encoded higher-order polarization state corresponds to $\Theta=\pi/2$, $\Phi=0$, and $l=3$, and its waist radius on the RGGD is $w_0=0.68$ mm.

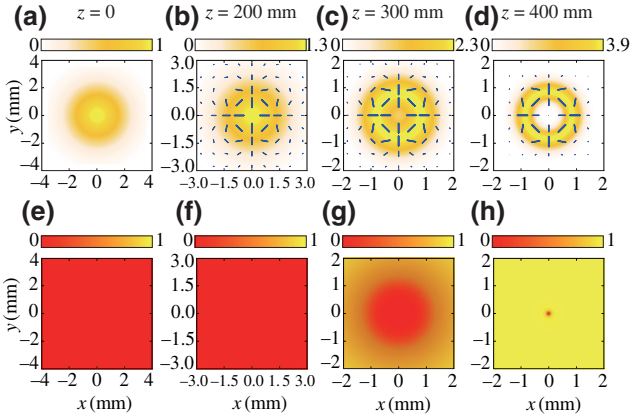


FIG. 7. Distributions of the simulated (a)–(d) intensity and polarization state (of the fully polarized part), and (e)–(h) the degree of polarization for a spatially partially coherent beam with encoded higher-order polarization state $\Theta=\pi/2$, $\Phi=0$, and $l=3$. The columns from left to right correspond to various distances from a thin lens (focal length $f=400$ mm). The intensity distributions in (a)–(d) are normalized by the maximum source-plane ($z=0$) intensity.

beam becomes more polarized and the higher-order polarization state shows up in the polarization state of the beam again. Notice that not all encoded higher-order polarization states imply an unpolarized source. We see by setting $\mathbf{r}_1=\mathbf{r}_2$ in Eq. (9) that the source is unpolarized if the integrals of $p_{xx}(\mathbf{v})$ and $p_{yy}(\mathbf{v})$ over the RGGD plane ($\mathbf{v}$ plane) are identical and that of $p_{xy}(\mathbf{v})$ equals zero.

### B. Propagation of the engineered partially coherent beam

Next we consider (paraxial) propagation of the prepared partially coherent electromagnetic beam in a stigmatic *ABCD* optical system. The setup is described by the transfer matrix with elements $A$, $B$, $C$, and $D$ [50]. It is shown within the Supplemental Material [40] that the polarization matrix after propagation can be obtained as

$$\Phi_{\alpha\beta}(\boldsymbol{\rho})=\frac{K_{\alpha\beta}}{(\lambda B)^2}|\tilde{F}(\boldsymbol{\rho}/\lambda B)|^2\otimes\tilde{\mu}_{\alpha\beta}(\boldsymbol{\rho}/\lambda B), \qquad (14)$$

with $(\alpha,\beta)\in(x,y)$. Above, the tilde $\tilde{}$ denotes the Fourier transform, $\otimes$ signifies the convolution, $F(\boldsymbol{\rho})=T(\boldsymbol{\rho})\exp(ikA\boldsymbol{\rho}^2/2B)$, and $\mu_{\alpha\beta}(\boldsymbol{\rho})$ is given in Eq. (11). The Fourier transforms of $F(\boldsymbol{\rho})$ and $\mu_{\alpha\beta}(\boldsymbol{\rho})$ are explicitly defined by Eqs. (S6) and (S12), respectively.

Next we apply Eq. (14) to analyze the propagation of a generated spatially partially coherent beam to which the higher-order polarization state of $\Theta=\pi/2$, $\Phi=0$, and $l=3$ is encoded. The beam is focused by a lens with the focal length of 400 mm and the beam characteristics are considered at various distances from the lens up to the focal plane. The simulated intensity, polarization state (of the fully polarized part), and the degree of polarization of the beam on propagation from the lens are shown in Fig. 7. We find that the dark core in the intensity gradually appears with the increase of propagation distance because the singularity forms in the higher-order polarization state. Moreover, we find from the spatial distributions of the degree of polarization [Figs. 7(e)–7(h)] that the degree increases with propagation distance. As shown in Fig. 7(h), the beam at the focal plane is effectively fully polarized within the beam area. Further, the polarization state in the focal plane coincides with the encoded higher-order state as evidenced by Fig. 7(d). Thus, the state encoded in the spatial coherence properties of a partially coherent source field is well reconstructed in the focal plane. We note that the maximum value in the scale bar for the intensity distribution increases with $z$ since the beam is now focused by the thin lens. By integrating over the intensity distributions in different planes, it is found that the energy of the beam during focusing is conserved.

Figure 8 shows the measured intensity and polarization state [(a)–(c)], as well as the degree of polarization [(d)–(f)] near the focal plane for the same beam as studied theoretically in Fig. 7. The polarization properties of the beam are measured in a standard manner [51]. We see that at the focal plane ($z=400$ mm) the beam exhibits the higher-order polarization state that was encoded in the spatial coherence of the source. Further, the degree of polarization increases with $z$ and the field is nearly fully polarized within the beam spot area in the focal plane. We notice that the global degree of polarization, defined as the

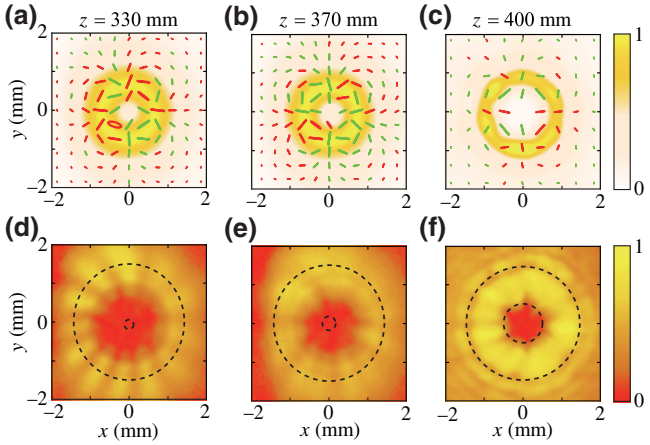


FIG. 8. Experimental results for the same encoded polarization state as in Fig. 7. (a)–(c) The measured intensity and polarization state (of the fully polarized part), and (d)–(f) the corresponding degree of polarization, at the distances of $z = 330$ mm [(a) and (d)], $z = 370$ mm [(b) and (e)], and $z = 400$ mm [(c) and (f)] from a lens with focal length $f = 400$ mm. Between the dashed rings in (d)–(f) the intensity is larger than 10% of its maximum value.

fraction of the beam power (intensity integrated over the beam cross section) carried by the fully polarized part, of the beam in the focal plane is closely linked to the spatial coherence width of the partially coherent source. We plot in Fig. 9 the behavior of the global degree of polarization on propagation for different spatial coherence widths of the source. It is found that the degree increases from 0 (completely unpolarized) in the source to a particular value (partially polarized) in the focal plane, and that the value increases with the decrease of the spatial coherence width. For the smallest spatial coherence width generated

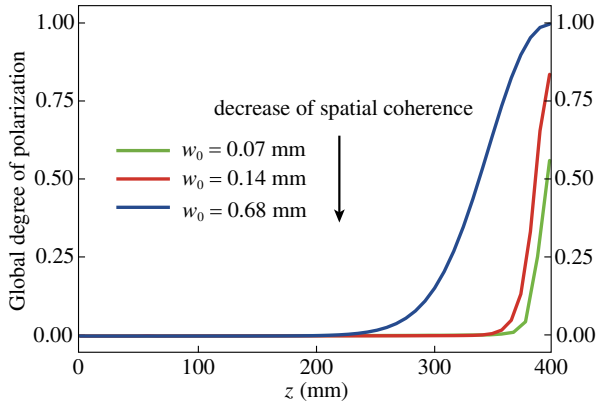


FIG. 9. Global degree of polarization of a partially coherent vector beam with different spatial coherence widths as a function of distance from the lens. The spatial coherence width is expressed with the waist radius $w_0$ on the RGGD. With the increase of $w_0$, the spatial coherence width decreases. The encoded polarization state is that of $\Theta = \pi/2$, $\Phi = 0$, and $l = 3$.

in our experiment (i.e., the beam waist on the RGGD is $w_0 = 0.68$ mm), the global degree of polarization (see blue curve in Fig. 9) in the focal plane can reach a value very close to one indicating that a highly polarized higher-order polarization state is generated.

### C. Large static obstacle in the beam

By now, we introduce a protocol that can encode a higher-order polarization state into the spatial coherence properties of a vectorial (secondary) light source and we show that the polarization state can be recovered in the far field (focal plane). Next, we examine the robustness of the generated beams. We first place a large static obstacle, i.e., a sector-shaped obstruction with closing angle $\phi = 7\pi/4$ to block part of the source beam and consider how well the higher-order polarization state can be recovered in the output plane. Figure 10 shows the simulated distributions of intensity, polarization state of the polarized portion [(a)–(d)], and the degree of polarization [(e)–(h)] for the same beam and in the same planes behind the lens as considered in Fig. 7, but with the presence of the obstacle. It is found that the higher-order polarization state gradually appears and the beam profile becomes dark hollow on propagation. Further, we see that the degree of polarization increases with the propagation distance. In the focal plane [Figs. 10(d) and 10(h)], a nearly fully polarized and high-quality higher-order polarization state is generated, which coincides with the encoded one. Compared with the blocked, spatially fully coherent beam in a higher-order

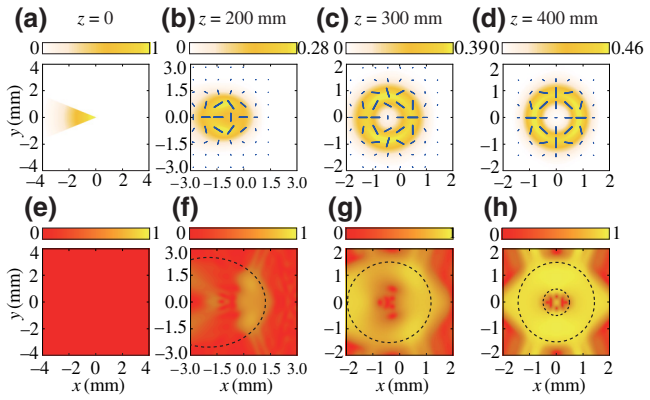


FIG. 10. The simulation results for (a)–(d) the intensity and the polarization state (of the fully polarized part), and (e)–(h) the degree of polarization for a spatially partially coherent vector beam at different planes behind a thin lens with focal length $f = 400$ mm. The encoded polarization state corresponds to $\Theta = \pi/2$, $\Phi = 0$, and $l = 3$ and the source-plane, sector-shaped obstacle has a closing angle of $\phi = 7\pi/4$. The intensity distributions in (a)–(d) are normalized by the maximum source-plane ($z = 0$) intensity. Inside the dashed rings in (f)–(h) the intensity is larger than 10% of its maximum value in the corresponding plane.

polarization state [cf. Fig. 2(f)], the approach of spatial coherence engineering shows super-strong robustness against disturbances.

The above simulations on beam propagation and focusing are based on Eq. (14) but with the function $F(\mathbf{r})$ replaced by $F(\mathbf{r}) = T(\mathbf{r})O(\mathbf{r})\exp(ikA\mathbf{r}^2/2B)$, where $O(\mathbf{r})$ denotes the transmission function of the obstacle in the source plane. We see from the convolution relation that when the spatial coherence of the source is very low, i.e., the Fourier transforms of the spatial correlation functions are much slower functions of the argument than the Fourier transform of $F(\mathbf{r})$, the focal-plane polarization matrix is determined mainly by the spatial coherence of the source, i.e., $\Phi_{\alpha\beta}(\boldsymbol{\rho}) \propto \tilde{\mu}_{\alpha\beta}(\boldsymbol{\rho}/\lambda B)$. In addition, it is found from Eq. (11) that the Fourier transform of $\mu_{\alpha\beta}(\mathbf{r}_1 - \mathbf{r}_2)$ is connected to the polarization state encoded in spatial coherence. Thus, a higher-order polarization state can be well mapped into the focal field although the beam is largely blocked in the source plane. We emphasize that the quality of the recovered polarization state is independent of the shape and the transverse position of the obstacle, since the spatial correlation functions depend uniformly on two-point difference in the source plane. The quality of the output polarization is determined by the relation between the spatial coherence area $S_c$ and the aperture area $S_o$ of the obstacle. When the condition $S_c \ll S_o$ holds, the polarization state can be well recovered in the focal plane. As shown in Figs. 6 and 10(a), the above condition holds in our simulation and experiment. We remark that the robustness against a blocking obstruction is independent of the encoded polarization state and any other state could have been used as well. As an example, simulations concerning specific polarization states with $l = 0$ and $l = 1$ can be found within the Supplemental Material [40].

In Fig. 11 we show the experimental results for the measured Stokes parameters and the recovered polarization state and degree of polarization in the focal plane for the beam analyzed computationally in Fig. 10. The experimental results in Figs. 11(d) and 11(e) are seen to be in good agreement with the simulation results in Figs. 10(d) and 10(h). Comparing the experimental result in Fig. 8(c) (without obstacle) with that in Fig. 11(d) (with obstacle), we find that the focal-plane intensity and polarization state are effectively unaffected by the large static obstacle placed in the propagation channel.

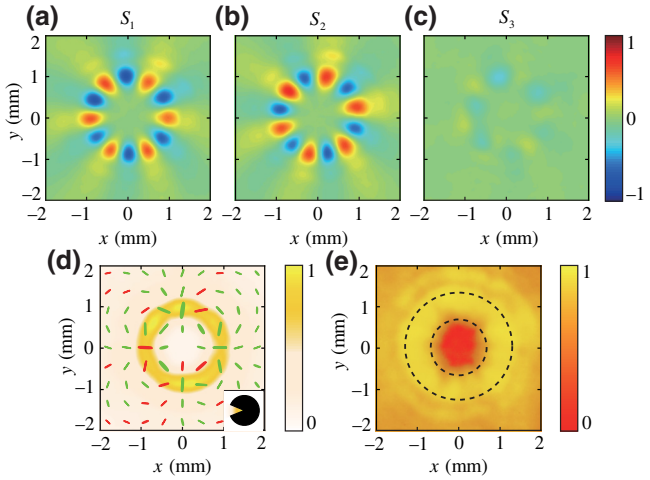


FIG. 11. Focal-plane distributions of the measured Stokes parameters (a) $S_1$, (b) $S_2$, and (c) $S_3$, and the recovered (d) polarization state, and (e) the degree of polarization of a partially coherent beam with the encoded polarization state $\Theta = \pi/2$, $\Phi = 0$, and $l = 3$. The source is blocked by a sector-shaped obstacle with the closing angle of $\phi = 7\pi/4$ [see inset in (d)]. Inside the dashed ring in (e) the intensity is larger than 10% of its maximum value and the focal length of the lens is $f = 400$ mm.

### D. Propagation through strongly fluctuating turbulence

We now turn to examine the robustness of the beams generated by our coherence-engineering protocol against fluctuating turbulence. In the simulations, the power spectrum for the atmospheric turbulence is that given in Eq. (4) and used in Fig. 4. We consider the propagation over 1 m under the strong turbulence ($C_n^2 = 5 \times 10^{-9}$ m$^{-2/3}$) with the details on the simulations relegated to the Supplemental Material [40]. Top panels in Fig. 12 show some simulated instantaneous intensity and polarization-state distributions of the beam propagated through the turbulence. It is seen that a high-quality higher-order (encoded) polarization state is formed in the output plane of the turbulence link. Furthermore, the beam spot is stable and unaffected by the turbulence. This is in striking contrast to the analogous distributions of the spatially fully coherent beam shown in Fig. 4.

The robustness of a partially coherent beam against turbulence can be explained as follows. A partially coherent beam can be viewed as a superposition of a set of random modes [52] in the time domain whose durations are $t_s$ (also named the characteristic time of a partially coherent beam). Typically $t_s$ is much smaller than the characteristic time $t_t$ of phase fluctuations induced by turbulence. The detector is chosen to be a "slow" detector for the random beam and a "fast" detector for the turbulence, i.e., the condition $t_s \ll t_d \ll t_t$ holds, where $t_d$ denotes the integration time of the detector. Thus, the instantaneous intensity and polarization state recorded by the detector in the output plane, exemplified by the simulation results in Figs. 12(a)–12(d), are averages over a large number of random modes. Furthermore, the size of the speckles in the random modes are determined by the spatial coherence of the partially coherent beam. With the decrease of spatial coherence width, the speckle size in the random modes decreases as well. Such random modes with smaller speckles are

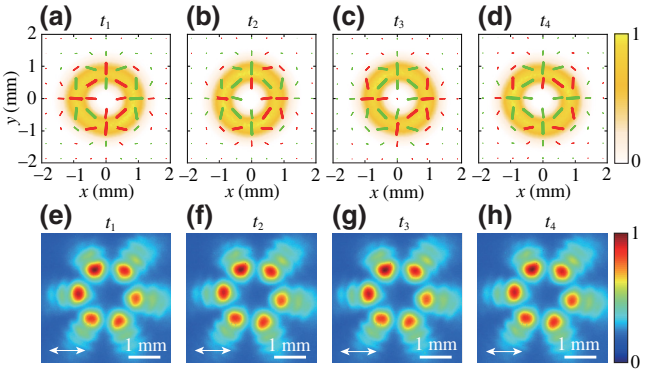


FIG. 12. Illustration of the effect of strong turbulence. (a)–(d) The simulated instantaneous intensity and polarization-state distributions of the beam propagated over 1 m in strong atmospheric turbulence with $C_n^2 = 5 \times 10^{-9}$ m$^{-2/3}$. (e)–(h) The experimentally obtained instantaneous intensity distributions of the $x$ component after passing through a thermally induced turbulence generated by a hot graphitic plate in 200 °C temperature. The encoded polarization state is specified by $\Theta = \pi/2$, $\Phi = 0$, and $l = 3$.

more robust against the turbulence than those with larger-scale speckle [40]. As with a static obstacle, the robustness against turbulence occurs independently of the encoded polarization state. For completeness and comparison, it is exemplified within the Supplemental Material [40] that the encoded radial and azimuthal polarization states ($l = 1$) are highly robust against the strong atmospheric turbulence with $C_n^2 = 5 \times 10^{-9}$ m$^{-2/3}$.

In our experiment, we pass the generated partially coherent beam through the same thermally induced turbulence as in Fig. 5. The characteristic time $t_t$ of the turbulence-induced phase fluctuations is about 40 ms when the temperature of the hot graphitic plate is 200 °C. The characteristic time of the partially coherent source is determined by the rotation speed of the RGGD and is about 5 $\mu$s. The integration time of the detector is set to 5 ms. Thus, the condition $t_s \ll t_d \ll t_t$ holds in our experiment. The bottom panels in Fig. 12 show the measured intensities (passed by an $x$ linear polarizer) in the output plane at four instants of time. It is found that the six-petal intensity distribution is highly stable in the output plane of a strong turbulence link.

## IV. CONCLUSIONS

In summary, we introduce a coherence-engineering protocol for encoding a higher-order polarization state into the spatial coherence characteristics of a partially coherent light source and show that the polarization state can be recovered in the far field with high global degree of polarization. In particular, we demonstrate both theoretically and experimentally that the constructed beams are highly robust against complex environments, represented in this work by a large static obstacle or strong atmospheric turbulence. In the first case, the encoded polarization state is recovered provided that the coherence area is much smaller than the aperture size. In the latter situation, the constructed random source is viewed as an incoherent superposition of random fields and the smaller is their speckle size (shorter coherence length in the source) the more unperturbedly the individual fields, after the turbulence link, exhibit the encoded information. Compared to the spatially fully coherent beams the engineered partially coherent vectorial light beams appear superior in transferring high-dimensional data encoded in the complex polarization states [9,10,27] through natural and harsh environments.

## ACKNOWLEDGMENTS

This research is supported by the National Key Research and Development Project of China (2019YFA0705000), the National Natural Science Foundation of China (NSFC) (Grant Nos. 11874046, 11974218, 11904247, 12192254, 12274310), the Innovation Group of Jinan (2018GXRC010), and the Academy of Finland (Grant Nos. 308393, 310511, PREIN 320166).

[1] D. H. Goldstein, *Polarized Light* (CRC Press, Boca Raton, 2011), 3rd ed.
[2] Q. Zhan, Cylindrical vector beams: from mathematical concepts to applications, Adv. Opt. Photon. **1**, 1 (2009).
[3] C. Rosales-Guzmán, B. Ndagano, and A. Forbes, A review of complex vector light fields and their applications, J. Opt. **20**, 123001 (2018).
[4] X. Xie, Y. Chen, K. Yang, and J. Zhou, Harnessing the Point-Spread Function for High-Resolution Far-Field Optical Microscopy, Phys. Rev. Lett. **113**, 263901 (2014).
[5] Y. Kozawa, D. Matsunaga, and S. Sato, Superresolution imaging via superoscillation focusing of a radially polarized beam, Optica **5**, 86 (2018).
[6] E. Otte and C. Denz, Optical trapping gets structure: Structured light for advanced optical manipulation, Appl. Phys. Rev. **7**, 041308 (2020).
[7] G. Milione, T. A. Nguyen, J. Leach, D. A. Nolan, and R. R. Alfano, Using the nonseparability of vector beams to encode information for optical communication, Opt. Lett. **40**, 4887 (2015).
[8] A. E. Willner, Vector-mode multiplexing brings an additional approach for capacity growth in optical fibers, Light: Sci. Appl. **7**, 18002 (2018).
[9] B. Ndagano, B. Perez-Garcia, F. S. Roux, M. McLaren, C. Rosales-Guzmán, Y. Zhang, O. Mouane, R. I. Hernandez-Aranda, T. Konrad, and A. Forbes, Characterizing quantum channels with non-separable states of classical light, Nat. Phys. **13**, 397 (2017).
[10] A. Sit, F. Bouchard, R. Fickler, J. Gagnon-Bischoff, H. Larocque, K. Heshami, D. Elser, C. Peuntinger, K. Günthner, B. Heim, C. Marquardt, G. Leuchs, R. W. Boyd, and E.

Karimi, High-dimensional intracity quantum cryptography with structured photons, Optica **4**, 1006 (2017).
[11] A. Forbes, A. Aiello, and B. Ndagano, Classically entangled light, Prog. Opt. **64**, 99 (2019).
[12] Y. Shen, I. Nape, X. Yang, X. Fu, M. Gong, D. Naidoo, and A. Forbes, Creation and control of high-dimensional multi-partite classically entangled light, Light: Sci. Appl. **10**, 50 (2021).
[13] G. Milione, H. I. Sztul, D. A. Nolan, and R. R. Alfano, Higher-Order Poincaré Sphere, Stokes Parameters, and the Angular Momentum of Light, Phys. Rev. Lett. **107**, 53601 (2011).
[14] A. Forbes, A. Dudley, and M. McLaren, Creation and detection of optical modes with spatial light modulators, Adv. Opt. Photon. **8**, 200 (2016).
[15] F. Cardano, E. Karimi, S. Slussarenko, L. Marrucci, C. De Lisio, and E. Santamato, Polarization pattern of vector vortex beams generated by q-plates with different topological charges, Appl. Opt. **51**, C1 (2012).
[16] F. Cardano, E. Karimi, L. Marrucci, C. De Lisio, and E. Santamato, Generation and dynamics of optical beams with polarization singularities, Opt. Express **21**, 8815 (2013).
[17] R. C. Devlin, A. Ambrosio, N. A. Rubin, J. P. B. Mueller, and F. Capasso, Arbitrary spin-to–orbital angular momentum conversion of light, Science **358**, 896 (2017).
[18] D. Naidoo, F. Roux, A. Dudley, I. Litvin, B. Piccirillo, L. Marrucci, and A. Forbes, Controlled generation of higher-order Poincaré sphere beams from a laser, Nat. Photon. **10**, 327 (2016).
[19] S. Vyas, Y. Kozawa, and S. Sato, Self-healing of tightly focused scalar and vector Bessel-Gauss beams at the focal plane, J. Opt. Soc. Am. A **28**, 837 (2011).
[20] G. Wu, F. Wang, and Y. Cai, Generation and self-healing of a radially polarized Bessel-Gauss beam, Phys. Rev. A **89**, 043807 (2014).
[21] W. Cheng, J. W. Haus, and Q. Zhan, Propagation of vector vortex beams through a turbulent atmosphere, Opt. Express **17**, 17829 (2009).
[22] M. A. Cox, C. Rosales-Guzmán, M. P. J. Lavery, D. J. Versfeld, and A. Forbes, On the resilience of scalar and vector vortex modes in turbulence, Opt. Express **24**, 18105 (2016).
[23] M. P. J. Lavery, C. Peuntinger, K. Günthner, P. Banzer, D. Elser, R. W. Boyd, M. J. Padgett, C. Marquardt, and G. Leuchs, Free-space propagation of high-dimensional structured optical fields in an urban environment, Sci. Adv. **3**, e1700552 (2017).
[24] J. Chen, L. Kong, and Q. Zhan, Demonstration of a vectorial optical field generator with adaptive close loop control, Rev. Sci. Instrum. **88**, 125111 (2017).
[25] Y. Dai, C. He, J. Wang, R. Turcotte, L. Fish, M. Wincott, Q. Hu, and M. J. Booth, Active compensation of extrinsic polarization errors using adaptive optics, Opt. Express **27**, 35797 (2019).
[26] Y. Zhai, S. Fu, J. Zhang, X. Liu, H. Zhou, and C. Gao, Turbulence aberration correction for vector vortex beams using deep neural networks on experimental data, Opt. Express **28**, 7515 (2020).
[27] Z. Zhu, M. Janasik, A. Fyffe, D. Hay, Y. Zhou, B. Kantor, T. Winder, R. W. Boyd, G. Leuchs, and Z. Shi, Compensation-free high-dimensional free-space optical communication using turbulence-resilient vector beams, Nat. Commun. **12**, 1666 (2021).
[28] Y. Cai, Y. Chen, and F. Wang, Generation and propagation of partially coherent beams with nonconventional correlation functions: a review (Invited), J. Opt. Soc. Am. A **31**, 2083 (2014).
[29] C. Liang, G. Wu, F. Wang, W. Li, Y. Cai, and S. A. Ponomarenko, Overcoming the classical Rayleigh diffraction limit by controlling two-point correlations of partially coherent light sources, Opt. Express **25**, 28352 (2017).
[30] Y. Shen, H. Sun, D. Peng, Y. Chen, Q. Cai, D. Wu, F. Wang, Y. Cai, and S. A. Ponomarenko, Optical image reconstruction in 4*f* imaging system: Role of spatial coherence structure engineering, Appl. Phys. Lett. **118**, 181102 (2021).
[31] Y. Chen, F. Wang, and Y. Cai, Partially coherent light beam shaping via complex spatial coherence structure engineering, Adv. Phys. X **7**, 2009742 (2022).
[32] D. Peng, Z. Huang, Y. Liu, Y. Chen, F. Wang, S. A. Ponomarenko, and Y. Cai, Optical coherence encryption with structured random light, PhotoniX **2**, 6 (2021).
[33] Y. Liu, Y. Chen, F. Wang, Y. Cai, C. Liang, and O. Korotkova, Robust far-field imaging by spatial coherence engineering, Opto-Electron. Adv. **4**, 210027 (2021).
[34] Y. Liu, X. Zhang, Z. Dong, D. Peng, Y. Chen, F. Wang, and Y. Cai, Robust Far-Field Optical Image Transmission with Structured Random Light Beams, Phys. Rev. Appl. **17**, 024043 (2022).
[35] S. Chen, X. Zhou, Y. Liu, X. Ling, H. Luo, and S. Wen, Generation of arbitrary cylindrical vector beams on the higher order Poincaré sphere, Opt. Lett. **39**, 5274 (2014).
[36] Y. Bao, J. Ni, and C.-W. Qiu, A minimalist single-layer metasurface for arbitrary and full control of vector vortex beams, Adv. Mater. **32**, 1905659 (2020).
[37] A. T. Friberg and T. Setälä, Electromagnetic theory of optical coherence [Invited], J. Opt. Soc. Am. A **33**, 2431 (2016).
[38] L. Mandel and E. Wolf, *Optical Coherence and Quantum Optics* (Cambridge University Press, Cambridge, 1995).
[39] J. M. Martin and S. M. Flatté, Intensity images and statistics from numerical simulation of wave propagation in 3-D random media, Appl. Opt. **27**, 2111 (1988).
[40] See Supplemental Material at http://link.aps.org/supplemental/10.1103/PhysRevApplied.18.034036 for the details of experiments for synthesizing a higher-order polarization state and encoding it to the spatial coherence distribution of a partially coherent beam. The derivation of the convolution expression in Eq. (14) is also shown. The simulation details for propagating a fully coherent and a partially coherent beam through an atmospheric turbulence are presented.
[41] X. L. Wang, J. P. Ding, W. J. Ni, C. S. Guo, and H. T. Wang, Generation of arbitrary vector beams with a spatial light modulator and a common path interferometric arrangement, Opt. Lett. **32**, 3549 (2007).
[42] A. M. Yao and M. J. Padgett, Orbital angular momentum: Origins, behavior and applications, Adv. Opt. Photon. **3**, 161 (2011).

[43] L. Allen, M. W. Beijersbergen, R. Spreeuw, and J. Woerdman, Orbital angular momentum of light and the transformation of Laguerre-Gaussian laser modes, Phys. Rev. A **45**, 8185 (1992),

[44] L. C. Andrews and R. L. Phillips, *Laser Beam Propagation through Random Media* (SPIE Press, Bellingham, 2005), 2nd ed. Chap. 3.

[45] F. Gori, V. Ramírez-Sánchez, M. Santarsiero, and T. Shirai, On genuine cross-spectral density matrices, J. Opt. **11**, 085706 (2009).

[46] Y. Chen, F. Wang, L. Liu, C. Zhao, Y. Cai, and O. Korotkova, Generation and propagation of a partially coherent vector beam with special correlation functions, Phys. Rev. A **89**, 013801 (2014).

[47] J. W. Goodman, *Statistical Optics* (John Wiley & Sons, New York, 1985).

[48] Z. Huang, Y. Chen, F. Wang, S. A. Ponomarenko, and Y. Cai, Measuring Complex Degree of Coherence of Random Light Fields with Generalized Hanbury Brown–Twiss Experiment, Phys. Rev. Appl. **13**, 044042 (2020).

[49] J. Tervo, T. Setälä, and A. T. Friberg, Degree of coherence for electromagnetic fields, Opt. Express **11**, 1137 (2003).

[50] S. A. Collins, Len-system diffraction integral written in terms of matrix optics, J. Opt. Soc. Am. **60**, 1168 (1970).

[51] P. Meemon, M. Salem, K.-S. Lee, M. Chopra, and J. P. Rolland, Determination of the coherency matrix of a broadband stochastic electromagnetic light beam, J. Mod. Opt. **55**, 2765 (2008).

[52] D. Voelz, X. Xiao, and O. Korotkova, Numerical modeling of Schell-model beams with arbitrary far-field patterns, Opt. Lett. **40**, 352 (2015).